

University of Massachusetts Amherst

From the Selected Works of Alfred Crosby

February 1, 2000

Deformation and Failure Modes of Adhesively Bonded Elastic Layers

Alfred Crosby, *University of Massachusetts - Amherst*

Kenneth R. Shull

Hamed Lakrout

Costantino Creton



Available at: https://works.bepress.com/alfred_crosby/26/

Deformation and failure modes of adhesively bonded elastic layers

Alfred J. Crosby, Kenneth R. Shull, Hamed Lakrout, and Costantino Creton

Citation: [Journal of Applied Physics](#) **88**, 2956 (2000); doi: 10.1063/1.1288017

View online: <http://dx.doi.org/10.1063/1.1288017>

View Table of Contents: <http://scitation.aip.org/content/aip/journal/jap/88/5?ver=pdfcov>

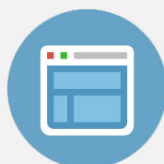
Published by the [AIP Publishing](#)

Advertisement:



Re-register for Table of Content Alerts

Create a profile.



Sign up today!



Deformation and failure modes of adhesively bonded elastic layers

Alfred J. Crosby and Kenneth R. Shull^{a)}

Department of Materials Science and Engineering, Northwestern University, Evanston, Illinois 60208-3108

Hamed Lakrout and Costantino Creton

Laboratoire de Physicochimie Structurale et Macromoléculaire, Ecole Supérieure de Physique et de Chimie Industrielles, Paris, France

(Received 1 February 2000; accepted for publication 7 June 2000)

Adhesively bonded elastic layers with thicknesses that are small relative to their lateral dimensions are used in a wide variety of applications. The mechanical response of the compliant layer when a normal stress is imposed across its thickness is determined by the effects of lateral constraints, which are characterized by the ratio of the lateral dimensions of the layer to its thickness. From this degree of confinement and from the material properties of the compliant layer, we predict three distinct deformation modes: (1) edge crack propagation, (2) internal crack propagation, and (3) cavitation. The conditions conducive for each mode are presented in the form of a deformation map developed from fracture mechanics and bulk instability criteria. We use experimental data from elastic and viscoelastic materials to illustrate the predictions of this deformation map. We also discuss the evolution of the deformation to large strains, where nonlinear effects such as fibrillation and yielding dominate the failure process. © 2000 American Institute of Physics.

[S0021-8979(00)00518-1]

I. INTRODUCTION

The mechanical response of thin, compliant layers is critically important in a variety of applications in several industries. Applications include protective layers in artificial hip joints,¹ underfills in flip chip technology,² and pressure-sensitive adhesives. In each of these applications, the robustness of the final products is largely dependent upon the integrity of the interface and the bulk properties of a thin, adhesively bonded, compliant layer. In addition, many products that are eventually useful as dry hard materials, such as paints, nail polish, concrete, or clay³ behave as soft materials at some point during their processing history. An understanding of the mechanical response of these systems is important as well. In all of these situations one must understand the physics controlling the integrity of compliant layers, in particular when a triaxial tensile stress is applied. To study the coupling of the bulk and interfacial properties that govern the failure of these layers, a variety of test geometries have been used. Among the more common test geometries are the peel test,^{4–6} the spherical (Johnson–Kendall–Roberts, or JKR) or flat (probe tack) techniques,^{7–10} and nanoprobe techniques [atomic force microscopy (AFM), nanoidentation].^{11,12} Illustrative schematics of the peel test and two of the probe geometries are shown in Fig. 1.

A variety of failure mechanisms are observed in these systems, depending on the detailed geometry and on the relevant materials properties. These failure mechanisms can range from simple interfacial fracture to cavitation leading to cohesive failure in a fibrillated structure.^{9,13–17} In all cases, the underlying physics is controlled by the coupling of bulk and interfacial properties of the thin layer. Qualitatively, this

coupling has been well described and quantitative advances have been made more recently.^{6,13,14,16–23} More work is still needed, however, to formulate a quantitative link between the overall mechanical performance and the properties of the compliant layer. This quantitative understanding of the bulk and interfacial contributions to performance is not only critical to predicting a product's engineering limits, but can also be used to optimize the design process for adhesive layers.

The geometric confinement of the compliant layer plays a dominant role in the determination of its mechanical response. In each of the applications mentioned above, the lateral dimensions of the compliant layer are significantly greater than its thickness. Consequently, as the layer is deformed in the thickness direction, lateral strains cannot be easily accommodated, and significant lateral stresses develop within the thin compliant layer. These stresses result in a substantial hydrostatic component in the stress field and play an important role in the response of the layer. The performance of the compliant layer is determined by its elastic modulus, its interfacial adhesion to the confining surfaces, and the degree of confinement. In this article, we use a simple analysis to develop a deformation map that can be used to predict the failure mechanism that is expected for a given combination of these parameters. These ideas are then tested with two viscoelastic materials that differ in their deviation from ideal elastic behavior.

II. DEFORMATION MODES

We begin by defining three main deformation modes that can be used to categorize the early stages of the debonding processes of a compliant layer from a rigid substrate. These three modes are described below, in the context of an axisymmetric testing geometry.

^{a)}Electronic mail: k-shull@nwu.edu

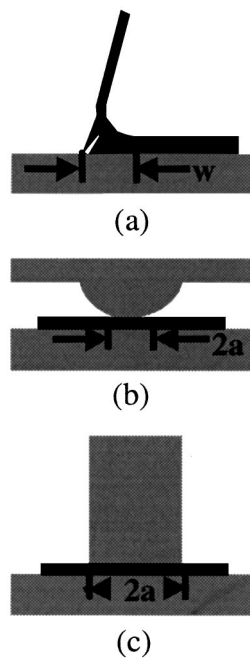


FIG. 1. Common geometries used to test the adhesive characteristics of thin layers. (a) Peel test; (b) spherical indenter; (c) flat cylindrical probe. The contact lengths over which stress is applied are shown in each case. In our analysis the compliant layer is assumed to be adhesively bonded to the substrate. For the cylindrical indenter (part c) the initial contact radius, a , is defined by the radius of the indenter, whereas for the spherical indenter (part b), the contact radius increases as the indenter is pushed into the compliant layer. The lateral dimensions of the thin, compliant layer are assumed to greatly exceed the contact radius for both of the axisymmetric geometries.

1. Edge crack propagation [Fig. 2(a)]. This failure mechanism is simple adhesive failure. The contact perimeter decreases uniformly as the compliant layer separates from one of the rigid substrates. The energy applied to the system is shared between propagating the interfacial crack and any viscoelastic losses in the bulk of the compliant layer. This mechanism of debonding can be effectively characterized using a fracture mechanics analysis.

2. Internal crack propagation [Fig. 2(b)]. In some situations, the hydrostatic stress at the interface develops to a point where a penny-shaped, internal crack will grow. If this defect remains at the adhesive/substrate interface, the growth of the penny-shaped crack is controlled by the same material properties controlling simple edge crack propagation. Typically, many internal cracks will nucleate and eventually coalesce when final failure occurs.

3. Cavitation [Fig. 2(c)]. This mode of deformation is similar to internal crack propagation, but the cavity expands into the bulk of the compliant layer instead of propagating at the interface. Growth of these bulk cavities corresponds to the early stages of fibrillation, which must take place in order for large deformations to be achieved.^{9,14,24}

In addition to these three main classes of deformation, the following two subclasses, related to the shape of the edge of the compliant layer, can also be defined.

1(a) Edge crack fingering. This failure mode is analogous to simple edge crack propagation with the exception that the contact perimeter does not decrease uniformly in all directions. Therefore the crack front does not appear as a

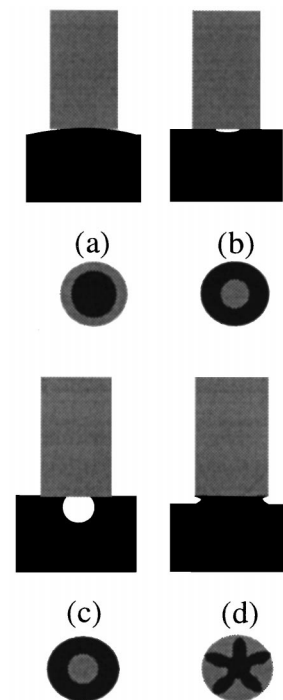


FIG. 2. The basic failure mechanisms observed in thin layers under normal loads: (a) Edge crack propagation; (b) internal crack propagation; (c) cavitation; (d) bulk fingering. Surface fingering is not shown, but is similar to bulk fingering, with the shape instability existing at probe/layer interface instead of within bulk of the compliant layer.

circle but has a more complicated geometry. This mechanism can no longer be analyzed in a straightforward way with fracture mechanics tools.

3(a) Bulk fingering [Fig. 2(d)]. Bulk fingering is visually similar to edge crack fingering. However, with bulk fingering the shape instability exists within the bulk of the compliant layer and not at the interface with the rigid indenter.^{17,25} Bulk fingering is closely related to cavitation, with the difference being that the cavity-type defect forms at the edge of the compliant layer. Once nucleated, these defects grow parallel to the adhesive/substrate interface. Cavitation and bulk fingering are treated as two manifestations of the same basic failure mode in this article. The bulk fingering mechanism shows a striking similarity to Saffman–Taylor fingers observed when a less viscous fluid displaces a more viscous one.²⁶ The driving force for the instability in the liquid case is the viscosity difference, while in our case it is the release of elastic stress.¹⁷ A similar analogy has been reported for the viscoelastic fracturing of colloidal fluids by injection of a fluid under high pressure.²⁷

The interfacial deformation modes (1, 1a, and 2) are governed by the energy release rate describing the driving force for crack propagation, whereas the bulk deformation modes (3 and 3a) are governed by the stress within the layer. The relationship between the average stress within the layer and the energy release rate is, in turn, determined by the degree of lateral confinement. This degree of confinement is defined by a representative dimension of the contact area in the stressed region, in comparison to the thickness of the compliant layer.^{8,16,28–30} For example, in a probe-type adhe-

sion test the degree of confinement is defined by the ratio of the contact radius (a) to the thickness of the layer (h); while in the peel test geometry, the degree of confinement is defined by the length of the stressed region (w) to the thickness of the adhesive layer (h). These quantities are illustrated in Fig. 1.

The origins of confinement effects can be illustrated by considering one of the axisymmetric probe geometries [Figs. 1(b) and 1(c)]. For low values of a/h there is a lateral Poisson contraction of the cylinder as it is extended.²⁹ As a/h increases, the lateral strains are restricted. These lateral constraints will dramatically alter the stress distribution within the sample and effectively increase its stiffness.^{29,31} For this reason, the sample will attempt to change its configuration to a more compliant geometry where less energy is required to strain the sample.¹⁷ This change in configuration is observed experimentally as one of the deformation mechanisms described above. In the following sections, we consider the specific case of a rigid flat or spherical punch in contact with an elastic layer of thickness, h [Figs. 1(b) and 1(c)].

A. Crack propagation

We begin with a fracture mechanics analysis that can be used to derive the driving forces for motion of an edge crack or internal crack. We assume a linearly elastic response for the compliant layer, in which case the driving force for propagation of an edge crack, G_{edge} , is given by the following expression:

$$G_{\text{edge}} = \frac{-(P' - P)^2}{4\pi a} \frac{dC}{da}, \quad (1)$$

where a is the contact radius, P' is the load required to establish this contact radius without adhesive forces, P is the experimental load, and C is the compliance of the system.^{16,19} G_{edge} represents the energy per area available to drive the crack forward, thereby reducing the contact area with the indenter and increasing the compliance. We use expressions for P' and for the compliance corresponding to full adhesive bonding, so that lateral shear stresses at both interfaces are not able to relax. Expressions for frictionless punches can also be used,¹⁶ although the adhesive boundary conditions are generally more representative of actual situations. For the flat probe geometry P' is equal to zero, while for the spherical probe geometry P' is given by the following equation:¹⁶

$$P' = \frac{4Ea^3}{3R(1-\nu^2)} \left(1 + 0.33 \left(\frac{a}{h} \right)^3 \right), \quad (2)$$

where E is the tensile elastic modulus, e , and ν is Poisson's ratio for the compliant layer, R is the radius of curvature for the indenter, and h is the original thickness of the compliant layer.

The compliance for both probe geometries (assuming $R \gg a$) is¹⁶

$$C = \frac{(1-\nu^2)}{2Ea} \left[1 + \left\{ \frac{0.75}{(a/h) + (a/h)^3} + \frac{2.8(1-2\nu)}{(a/h)} \right\}^{-1} \right]^{-1}. \quad (3)$$

From this expression, assuming that the material is incompressible ($\nu=0.5$), the driving force for edge crack propagation is¹⁶

$$G_{\text{edge}} = \frac{9(P' - P)^2}{128\pi Ea^3} \frac{\{0.75 + 2(a/h) + 4(a/h)^3\}}{\{0.75 + (a/h) + (a/h)^3\}^2}. \quad (4)$$

When the crack actually propagates the energy represented by G_{edge} is expended by the creation of new surfaces and in viscoelastic losses near the crack tip. These viscoelastic losses depend on the crack velocity, v ($v = -da/dt$), so that the rate of edge crack propagation is determined by a material dependent relationship between G_{edge} and v . The following empirical relationship between these quantities has often been used:^{13,16–21}

$$G = G_0 \left(1 + \left(\frac{v}{v^*} \right)^n \right) \quad (5)$$

or

$$v = v^* \left(\frac{G}{G_0} - 1 \right)^{1/n}.$$

Note that G_0 is the initial energy release rate required to begin crack movement and that the velocity dependence is parametrized by v^* and n . In an ideally elastic material, v^* would be infinite and the fracture criteria would not be velocity dependent, but rather one critical energy release rate, G_0 , would act as the fracture criterion.

The relation shown in Eq. (5) also acts as a failure criterion for internal, penny-shaped cracks. For a homogeneous medium under a state of uniaxial tensile stress, the energy release rate characterizing a penny-shaped crack is given by the following expression:^{32,33}

$$G_{\text{cavity}} = \frac{4(1-\nu^2)\sigma^2}{\pi E} a_c, \quad (6)$$

where σ is the far-field tensile stress and a_c is the radius of the crack. For an interfacial crack at a rigid, frictionless surface, G_{cavity} will be half the value given by Eq. (6) because there is no elastic strain energy in the rigid substrate. Quantitative use of Eq. (6) in our case is complicated by the adhesive boundary condition (the interface on which the crack grows is not frictionless), and by the triaxial state of stress in these confined systems. Nevertheless, Eq. (6) can be used as a qualitative measure of the driving force for the early stages of internal crack propagation, where a_c is much smaller than a or h .

A last interfacial fracture mechanism that should be briefly mentioned is the propagation of finger-like cracks starting from the edge of the probe inwards. This mechanism has been observed for very confined layers ($a/h = 50-100$) on a substrate with a very low adhesion.³⁴ The driving force is also the release of elastic stress, but the confinement can be reduced more effectively by the propagation of finger-like cracks. In this case the applied energy release rate varies along the contact perimeter, and cannot be readily quantified by Eq. (4).

A further assumption implicit in the use of Eqs. (4) and (6) for the energy release rate is that the compliant material

has a predominantly elastic character. In other words, the volume of material associated with viscoelastic loss must be localized near the crack tip and must be much smaller than the total strained volume. Under these conditions, the averaged response of the adhesive system will be elastic. When these conditions do not apply, a modified fracture mechanics formulation is required.³⁵

If the applied energy release rate [Eqs. (4) and (6)] exceeds G_0 , then the corresponding crack will propagate at a velocity given by Eq. (5). For an edge crack, propagation decreases a , resulting in a more compliant system as described by Eq. (3). Propagation of internal cracks is also driven by the resulting increase in the compliance. However, for highly confined systems the change in compliance per change in unit area is very small. Therefore, other means of releasing lateral constraint will dictate the deformation mode. These deformation modes are cavitation and bulk fingering, as described in the following section.

B. Cavitation and bulk fingering

Until this point, we have focused on the criteria for interfacial failure, which is quantified by the energy release rate. As the applied energy release rate increases so do the stresses in the bulk of the thin layer. If these stresses reach a critical point, the lateral constraint will be relieved as an elastic instability. The most straightforward instability is cavitation within the compliant layer [Fig. 2(c)]. Gent has described cavitation in terms of the growth of a preexisting cavity in a material obeying the simple kinetic theory of elasticity.¹⁵ The relationship between the size of the cavity and the magnitude of the far field hydrostatic stress is given as follows:¹⁵

$$\sigma_{\text{hyd}} = E\{(5 - 4\lambda^{-1} - \lambda^{-4})/6\}, \quad (7)$$

where λ is the ratio of the actual cavity radius to the cavity radius in the unstressed state. Note that this simple treatment does not account for the energy penalty of creating new surface area or for the finite extensibility of the rubber. Based on Eq. (7), if the hydrostatic stress within a material becomes greater than $5E/6$ then the cavity will be energetically driven to grow ($\lambda \rightarrow \infty$).¹⁵ As in the case of an interfacial crack propagation, the growth of cavities releases lateral constraints, thereby increasing the compliance of the system.¹⁷ The distinguishing feature of cavity growth is that the contact area with the probe is not changing as this process occurs.

Bulk fingering is another form of a bulk elastic instability, but in this case the “cavity growth” occurs on the edge of the sample volume and not in the interior [Fig. 2(d)].^{17,25} Although an exact criteria for the occurrence of fingering has not been determined, the origins of this phenomenon can also be traced to the release of lateral constraints within the compliant layer.¹⁷ Experiments have confirmed that the initial driving force is elastic and that finger formation typically occurs prior to cavitation.¹⁷ Note that the maximum length of the bulk fingers is limited by the thickness of the compliant layer, so that they might not be discernible for very high values of a/h . For example, if the maximum strain that an

elastomer can accommodate without failure is assumed to be 3.0, then the maximum length of the fingers [as shown in Fig. 2(d)] is $3.0 \cdot (h/2)$, where h is the thickness of the compliant layer. Therefore, if we assume a typical thickness to be $100 \mu\text{m}$, then the maximum finger length would be $150 \mu\text{m}$. Consequently, this length would only occupy 3% of a 0.5 cm radius probe. Under these conditions, internal cavitation will be the dominant bulk deformation mode.

C. Transition from interfacial to bulk deformation modes

Now that we have discussed the individual criteria for interfacial and bulk deformation modes, we can combine the arguments to understand how the degree of confinement, the elastic properties of the layer (represented for the sake of simplicity by the Young's modulus E), and the relationship between G_{edge} and the crack propagation velocity (represented here by the threshold value G_0) control the initial stages of failure. As the force (P) on the adhesive layer increases, the hydrostatic stress in the bulk of the adhesive and the applied energy release rate [given by Eqs. (4) and (6)] also increase. The first of these quantities to surpass its respective failure criterion will determine which failure mechanism prevails.

We can define a general set of criteria and a corresponding map of preferred failure mechanisms if we rearrange Eqs. (4) and (6). First, we define an average normal stress, σ_{avg} , as follows:

$$\sigma_{\text{avg}} = \frac{P}{A}, \quad (8)$$

where A is the contact area. For a flat probe ($P' = 0$), the expression for G_{edge} [Eq. (4)] can be written in the following form:

$$\frac{G_{\text{edge}}}{Ea} = \frac{9\pi}{128} \left(\frac{\sigma_{\text{avg}}}{E} \right)^2 \left[\frac{\{0.75 + 2(a/h) + 4(a/h)^3\}}{\{0.75 + (a/h) + (a/h)^3\}^2} \right]. \quad (9)$$

If G_{edge} surpasses G_0 , then edge crack propagation will occur. However, if σ_{avg}/E reaches a value of approximately one, then a bulk elastic instability will release the lateral constraint. Note that G_{edge} depends on two geometrical parameters: the degree of confinement (given by a/h) and a size parameter (given by a).

We can also develop an expression based on Eq. (6) for the early stages of internal crack propagation. By approximating σ by σ_{avg} , and by dividing by a factor of 2 to take into account the fact that crack propagation occurs at the interface with a rigid solid, we obtain the following:

$$\frac{G_{\text{cavity}}}{Ea} = \frac{2(1 - \nu^2)}{\pi} \left(\frac{\sigma_{\text{avg}}}{E} \right)^2 \left(\frac{a_c}{a} \right). \quad (10)$$

This expression is valid for $a_c \ll a$ and $a_c \ll h$, in which case G_{cavity} is dependent on a single geometric parameter, a_c . If σ_{avg}/E exceeds a critical value close to one, an interfacial defect will expand into the bulk of the compliant layer as illustrated in Fig. 2(c).¹⁵ Note that our qualitative treatment does not take into account the shape of the stress distribution, which depends on a/h , the compressibility of the compliant

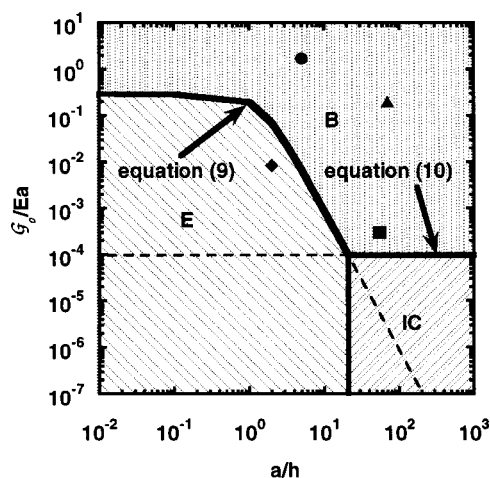


FIG. 3. Deformation map for $\nu=0.5$ and $a_c/a=2\times 10^{-4}$, illustrating the effect of confinement on the preferred failure mechanism exhibited by a thin layer under normal loads. Three regions are distinguished corresponding to the preferred deformation mode: edge crack propagation occurs within region E; internal crack propagation occurs within region IC, and bulk instabilities (either cavitation or bulk fingering) occur within region B. The four individual data points refer to the following tests, using the parameters listed in Table II: (◆) D/T with spherical indenter; (■) D/T with flat indenter; (●) PEHA with spherical indenter; (▲) PEHA with flat indenter.

layer, and the radius of curvature of the rigid punch.^{14,17,36} Finally, we neglect differences between the hydrostatic stress and the normal stress which become significant at low values of a/h . While these factors affect the detailed response of the system, including the distribution of cavitation or internal crack growth within the contact area, they do not affect the general features of the deformation process. As described below, one can predict which deformation mechanism will initially be active if G_0/Ea , a/h , and the defect size, a_c , are known.

If we assume that bulk instabilities will occur for $\sigma_{\text{avg}} > E$, that internal crack growth will occur for $G_{\text{cavity}} > G_0$, and that edge crack growth will occur for $G_{\text{edge}} > G_0$, we can define a deformation map by setting σ_{avg}/E equal to one in Eqs. (9) and (10) and plotting G_{cavity}/Ea or G_{edge}/Ea as a function of the degree of confinement (a/h). These two lines, and the vertical line extending downward from their intersection, divide the map into different regions as illustrated in Fig. 3. This map corresponds to the case where $a_c/a=2\times 10^{-4}$, $a_c/h \ll 1$, and where the sample is incompressible ($\nu=0.5$). The assumption of a small defect is valid for most practical applications where the initial defect size is related to the surface roughness of the two contacting bodies and is very small relative to the overall sample dimensions.^{37,38}

Although the details of the deformation map depend on the specific value of σ_{avg}/E chosen for the bulk instability criterion, the general physics defined in this plot are quite reliable. Three different regions are defined in Fig. 3: (1) Edge crack propagation (E), (2) Bulk instabilities (B), and (3) Internal crack propagation (IC). In the “E” region, the energy release rate for edge crack propagation (curved line) is greater than the energy release rate for internal crack propagation (horizontal line). Also in region E, the stress

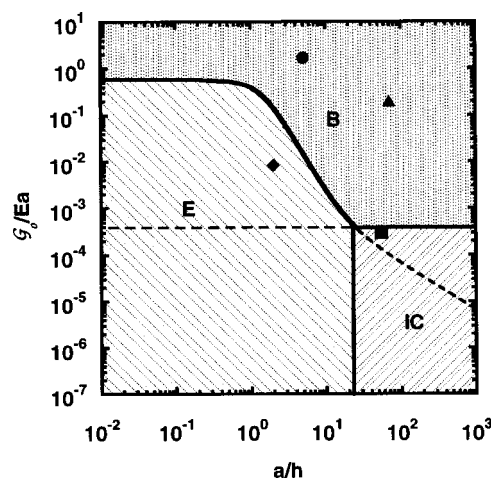


FIG. 4. Deformation map for $\nu=0.499$ and $a_c/a=8\times 10^{-4}$. The symbols are identical to those shown in Fig. 3.

applied to the sample is less than the stress required to induce a bulk elastic instability. Therefore, edge crack propagation will dominate as the initial failure mechanism if the degree of confinement (characterized by a/h) and the material's resistance to crack propagation (characterized by G_0/Ea) place the experimental conditions within this region. If the resistance to crack propagation is sufficiently large, one can access region “B” on the map, where the stresses on the compliant layer are high enough to result in an elastic shape instability. As the degree of confinement increases, the extent of region B grows. In the “IC” region, the driving force for growth of an internal crack (horizontal line) exceeds the driving force for an edge crack (sloped line), but the tensile stress is too low to extend the cavity into the bulk of the adhesive.

The general form of Eq. (9) for different values of Poisson's ratio can be found by combining Eqs. (1), (3), and (8).¹⁴ Increasing the compressibility of the compliant layer (decreasing ν) increases G_{edge} , whereas increasing a_c increases G_{cavity} . Both of these changes decrease the extent of the region corresponding to bulk instabilities on the deformation map. These effects are illustrated in Fig. 4, where we show a second deformation map corresponding to $\nu=0.499$ and $a_c/a=8\times 10^{-4}$.

We are now in a position to consider how the degree of confinement and the sample size affect the deformation mechanism. Figure 3 demonstrates that as the degree of confinement increases, edge crack propagation becomes less likely and internal deformation modes dominate. At lower degrees of confinement, edge crack propagation will always occur except when the adhesive strength is significantly greater than E^*a . These general features can be very useful for some common applications of adhesively bonded elastic layers. In order to make a prediction one needs to measure or estimate G_0 for the interface, E of the soft material, and three characteristic sizes a , h , and a_c . Then:

(1) The value of a_c/a allows the correct positioning of the transition from internal crack propagation to edge crack propagation.

(2) The values of G_0/Ea and a/h define the appropriate

location on the deformation map, and determine which deformation mode will be favored.

As an example, we can use our map to predict how underfill materials in flip-chip packages will fail under an applied stress normal to the substrate interface. Based on typical geometries and material properties, a/h is approximately one and E^*a is equal to 31×10^4 J/m² for most underfill applications.² As long as the fracture strength, G_0 , of the interface is less than 9.5×10^4 J/m² (which is unrealistically high for polymer/substrate adhesion strengths), edge crack propagation is the predicted failure mode. Formation of a bulk instability is only possible when a much more compliant adhesive layer, typical of that used for a pressure sensitive adhesive, is used. As we will demonstrate experimentally, the release of lateral constraint through bulk instabilities can allow configurations to be obtained where yield stresses are surpassed so that much larger amounts of energy are dissipated.

Another interesting prediction from our map applies to the recent trend of using scanning probe microscope geometries to investigate adhesive properties of soft polymers on a submicron scale, but still in a regime where continuum mechanics can apply. In these tests, the typical tip geometry limits the maximum contact radius to be no larger than 100 nm. With this radius and assuming that the material being investigated has an elastic modulus of 1.0 MPa, our map predicts that bulk instabilities will always occur if the critical fracture energy exceeds 0.03 J/m². This value of 0.03 J/m² is very small considering that the lower bound for fracture energies, the thermodynamic work of adhesion, is typically close to 0.1 J/m² for elastomers. The predicted importance of bulk instabilities is a simple consequence of the average stress defined by Eq. (8) becoming very large as the contact area becomes small. In other words, as a becomes very small relative to G/E and h , surface energetics dominate the volume effects and some form of bulk instability is likely to occur before the interfacial attraction is overcome. With these predictions in mind, extreme care must be taken as adhesive strengths are quantified from nanoscale measurements. One must remember, however, that our simple treatment neglects the effects of the surface energy and the associated Laplace pressure. These effects also become important at small length scales, and will act to suppress the development of a bulk shape instability.

With the map presented in Fig. 3 and the underlying Eqs. (9) and (10), we now have the tools to begin to quantitatively understand why certain modes of failure will dominate under certain states of confinement. To illustrate the use of these proposed tools, we examine the experimental results of two material systems collected for two significantly different states of confinement. One material behaves mostly elastically, while the other material has a strong viscous contribution to its mechanical behavior.

III. EXPERIMENT

A. Adhesion tests

The spherical and flat probe geometries illustrated in Fig. 1 were used in our experiments, depending on the values

TABLE I. Experimental parameters for (a) D/T samples; (b) PEHA samples.

Material Geometry	D/T		PEHA	
	Flat	Spherical	Flat	Spherical
h (μm)	91	91	71	121
R (mm)	∞	6.0	∞	3.2
Indenter material	Steel	Glass	Steel	Steel
Motor velocity ($\mu\text{m/s}$)	2.5	2.5	10	8.6

of a/h that were desired. As described in previous references, values of a/h from 1 to 5 are readily obtained with a spherical indenter, and values as large as 100 are obtained with a flat cylindrical punch.^{14,16,39}

The general technique for both geometries begins by bringing the probe into contact with the polymer layer until a previously set arbitrary load is detected by the load transducer. At this point of maximum compression, the probe waits at fixed displacement for a prescribed dwell time. Following the dwell time, the probe is pulled away from the adhesive layer. During this pull-off stage, the force, displacement, and contact area are recorded at regular intervals. Pull-off continues until final failure occurs. Specific test parameters are presented in Table I for both material systems and for both geometries.

In addition to the adhesive testing, a rheometric technique has been employed to collect the rheological data for the polymer layer. This technique has been custom designed to accurately measure the rheological properties of confined polymer samples. This method involves bringing a hemispherical indenter into contact with a thin adhesive layer. At a fixed contact area, we then apply an oscillatory strain in the normal direction. By measuring the magnitude of the resulting stress and the phase lag between the stress and the applied strain, we can calculate the storage and loss moduli for the polymer layer.

B. Materials

The two material systems investigated in this report are referred to as D/T and PEHA. D/T is a blend of poly(*n*-butyl acrylate)—poly(methylmethacrylate) (PMMA) diblock and poly(methylmethacrylate)-poly(*n*-butyl acrylate)-poly(methylacrylate) triblock copolymers. The details of the anionic polymerization of these molecules have been presented previously.^{40,41} The molecular weight of the triblock is 167 000 g/mol (82 wt% PnBA) with a polydispersity of 1.12. The diblock molecules correspond to 35% by weight of the overall polymer and are half as large as the triblock molecules. Also, the PnBA segments contain approximately 4% acrylic acid groups. The rheological data for this polymer are presented in Fig. 5. These data were collected using the axisymmetric contact mechanics technique described above. The general trends to observe are that the storage modulus is

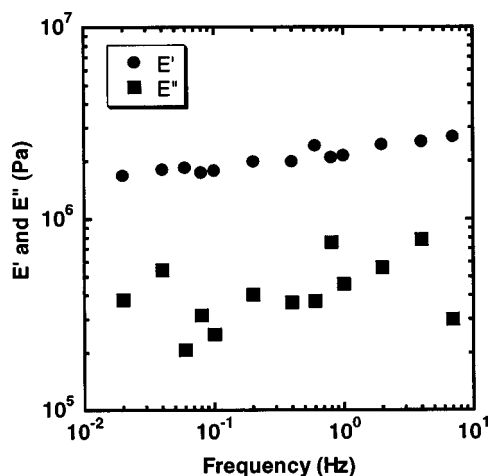


FIG. 5. Rheological data for D/T. E' is the storage modulus and E'' is the loss modulus. Data were collected using custom-designed contact mechanical geometry at room temperature with an imposed strain of 5.5%.

weakly dependent upon frequency and significantly greater than the loss modulus. This behavior indicates that D/T is a mostly elastic material.

As a complement to the predominantly elastic D/T, we use PEHA, which is a homopolymer of poly(2-ethylhexyl acrylate). This polymer has a very broad molecular weight distribution and has a rheological signature characteristic of a polymer near its gel point as illustrated in Fig. 6. The storage and loss moduli are roughly equal to one another and exhibit a power law frequency dependence. These data were collected using a conventional parallel plate shear rheometer.

C. Sample preparation

A gel-casting method is used to prepare the D/T layers for the mechanical measurements.⁴² With this method, a 5 vol % polymer solution is made by dissolving the polymer in warm 2-ethylhexanol ($T > 70^\circ\text{C}$). The solution is then

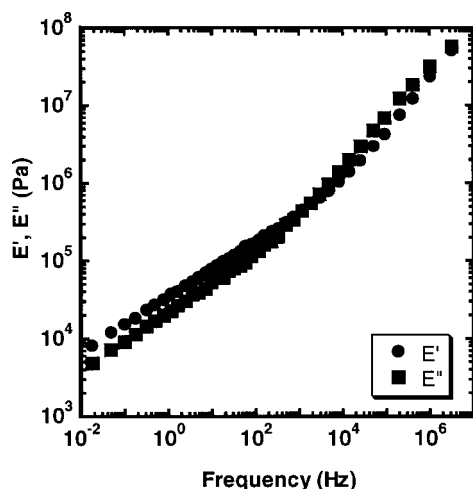


FIG. 6. Rheological data for PEHA. E' is the storage modulus and E'' is the loss modulus. Data were collected on a parallel plate shear rheometer at a spectrum of temperatures and frequencies. Time-temperature superposition was used to shift data curves to form a master curve for room temperature (25°C).

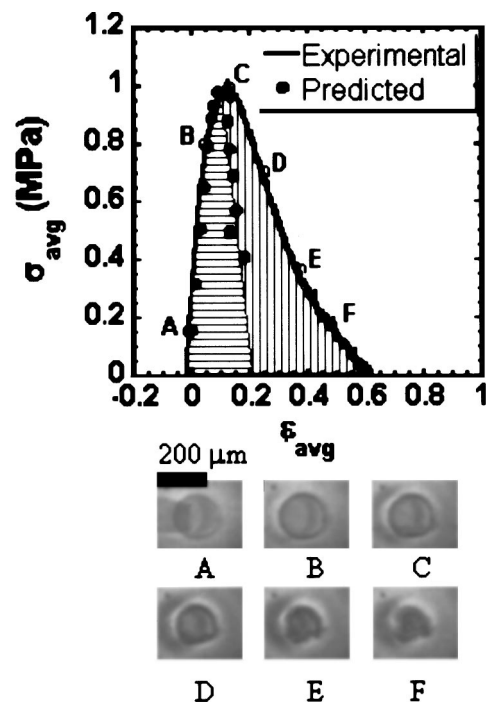


FIG. 7. Average stress-strain curve for a spherical indenter test on D/T. The maximum a/h is 2.0. Images correspond to the points indicated on the stress-strain curve. Predicted stress-strain curves for D/T are also shown. Horizontal line shading corresponds to estimate of elastic energy used to drive the interfacial crack. Vertical line shading indicates estimated energy dissipated due to yielding in the sample volume.

cooled to room temperature. During the cooling process, the PMMA end blocks aggregate to form a physically crosslinked gel.⁴² A small quantity of the gel is molded onto a glass slide to give a layer of known thickness. This gel layer is then dried at room temperature for several days until all of the solvent is removed. During this drying stage, the gel network remains intact, thus forming a mostly elastic adhesive layer. Details of the gel microstructure, the effects of drying, and the advantages of gel casting over solution casting have been given by Flanagan, Crosby, and Shull.⁴²

The PEHA samples were prepared by depositing a small quantity of latex onto a glass slide and doctor blading the quantity of sample to achieve a uniform film. This latex layer is then dried at room temperature and annealed for 4 h at 70°C under vacuum.

IV. RESULTS AND DISCUSSION

A. Adhesive failure analysis of elastic system

Figure 7 shows the average-stress versus average-strain curve for a representative adhesion test using the spherical probe geometry on the D/T adhesive. The average stress is defined as the force normalized by the maximum contact area and the average strain in the displacement divided by the original thickness of the adhesive layer. Along with the stress-strain curve, we have included images of the contact area at specific points during the test. The maximum value of a/h for this test is 2.

As can be seen from the images, the contact area remains mostly circular during the entire bonding and debond-

ing phases. This mode of failure corresponds to edge crack propagation [Fig. 2(a)] and allows us to use elastic fracture mechanics to calculate the adhesive failure criteria for this polymer/substrate combination. To verify the assumption of linear elasticity that is fundamental to the fracture mechanics relation shown in Eq. (4), we first use a curve fitting technique with the elastic modulus as a fitting parameter.^{13,16} For a material that is acting in a linear elastic manner, the compliance is given by the following relation:

$$C = \frac{\delta' - \delta}{P' - P}. \quad (11)$$

This relation can be rearranged to predict a displacement with the appropriate substitutions made for δ' , P' , and C

$$\delta = \delta' - C(P' - P), \quad (12)$$

where P is the experimental load, C is equal to the expression in Eq. (3), and P' is given by Eq. (2). The expression for δ' is¹⁶

$$\delta' = \frac{a^2}{R} [0.4 + 0.6 \exp(-1.8(a/h))]. \quad (13)$$

We use the elastic modulus, E , as the single fitting parameter to find the best-fit curve for our experimental force-displacement curve. The best-fit average stress-strain curve is shown in Fig. 7 where the value for E is 2.0 MPa. This modulus agrees with the rheological data in Fig. 5. Evidently, after the maximum tensile point is reached, our predicted values for average strain underestimate the actual average strain in our sample. Our interpretation of this result is that the extra strain represents inelastic deformation, and that the strained volume of the adhesive has exceeded its yield point.

Given that our D/T system is acting in a linearly elastic manner during the initial portions of the test, we can use Eq. (4) to calculate the energy release rate. As mentioned in the section on failure criteria, the energy release rate should be related to the crack tip velocity. From the contact radius measurements as a function of elapsed time, we can find the crack tip velocity and determining the three parameters used in Eq. (5) to describe the interfacial properties: G_0 , v^* , and n . G_0 , or the minimal energy release rate required to initiate measurable crack propagation, is approximately 3.0 J/m², while the largest value of G applied to the interface is about 13 J/m². The quantities of v^* and n are equal to 1.8 $\mu\text{m/s}$ and 0.7, respectively.

Based on the adhesive failure criteria that we measured using the spherical probe test, we can verify our arguments for the dominant failure modes. Using Fig. 3, we find that for the D/T sample at an a/h value of 2.0 and a G_0/Ea value near 8×10^{-3} ($G_0 \approx 3 \text{ J/m}^2$, $E \approx 2 \times 10^6 \text{ Pa}$, $a \approx 2 \times 10^{-4} \text{ m}$) the preferred mode of failure should be edge crack propagation as was observed in the images in Fig. 7.

To achieve large degrees of confinement, the most effective test geometry is the flat probe. The average-stress versus average-strain results for a D/T sample are shown in Fig. 8. During this test, a maximum a/h value of 55 was achieved. As predicted by Fig. 3, the observed mode of failure is no longer edge crack propagation, but rather internal cavitation.

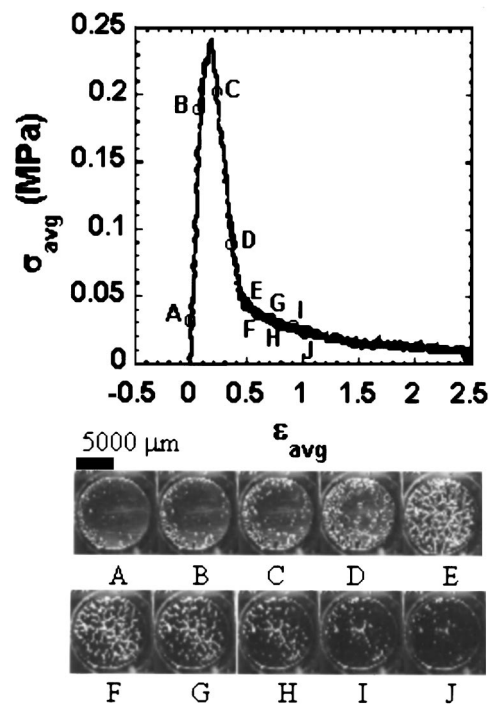


FIG. 8. Average stress-strain curve for a flat indenter test on D/T. The maximum a/h is 55.0. Images correspond to the points indicated on the stress-strain curve.

This cavitation mechanism is illustrated in the images shown in conjunction with the stress-strain curve in Fig. 8.

In addition to experimentally verifying our conclusions on failure criteria, these results for different degrees of confinement on the same adhesive sample can be used to illustrate how the same material physics drive the adhesive failure in both the spherical and flat probe geometries. The total dissipated energy normalized by the maximum contact area (W_{adh}), the maximum tensile stress, and the maximum tensile strain are common parameters used to evaluate probe-type adhesion tests. The values for these parameters are listed in Table II for both the flat and spherical geometry tests conducted on the D/T adhesive.

The most striking comparison is between the values of W_{adh} . One might initially assume that if the interfacial fracture criteria is roughly the same in both tests, then the amount of dissipated energy per unit area should be similar for both test geometries. However, as Table II shows, nearly

TABLE II. Results obtained with the two different adhesives with each of the two test geometries. Values of G_0 , E , Max a , and Max a/h were used to locate the four different tests on the deformation map (Figs. 3 and 4).

Material	D/T		PEHA	
	Flat	Spherical	Flat	Spherical
W_{adh} (J/m ²)	9.75	27.6	20.37	17.5
σ_{max} (MPa)	0.242	1.03	0.37	0.034
ϵ_{max}	2.49	0.629	2.73	8.46
G_0 (J/m ²)	3.0	3.0	10.0	10.0
E (MPa)	2.0	2.0	0.01	0.01
Max a (μm)	5000	180	5000	600
Max a/h	55	2.0	70	5.0

three times the amount of energy per unit area is dissipated in the spherical probe test. Our explanation for this result is that for the D/T adhesive failure occurs by internal crack propagation for the flat probe geometry and by edge crack propagation for the spherical probe geometry. As illustrated by Fig. 3, the increased value of the contact radius for the flat probe moves this test into the IC region (interfacial crack propagation) of the deformation map, assuming $a_c = 4 \mu\text{m}$ ($a_c/a = 8 \times 10^{-4}$) and $\nu = 0.499$. Lateral constraints are relieved in this sample by rapid propagation of these internal cracks (images C through E of Fig. 8). This release of elastic energy prevented the average stress σ to ever increase above E. Finally all the cracks coalesced together and the entire contact area debonded within a very short period of time (images F through I of Fig. 8). Due to the high degree of confinement and to the high modulus, lateral constraints were released very early by internal crack propagation and the stresses within the polymer layer were never allowed to develop past the point of yield.

In contrast, during the spherical probe test, the degree of confinement was considerably lower, thus causing the primary means of failure to follow edge crack propagation. The rate at which the edge crack allowed lateral constraints to be released was not great enough to prevent the stresses within the strained volume from surpassing the yield point. This statement is most strongly supported by the discrepancy between the measured and predicted displacements for large strains. At stresses beyond the yield stress of the adhesive layer, the constitutive relation for this layer can no longer be described by linear elasticity. Once the yield point of the adhesive is exceeded, part of the applied energy is lost to inelastic deformation. Through an informal argument, we can use our linear elastic fracture mechanics relations to separate the fraction of energy that was used to drive the crack from the fraction that was dissipated in the yielded material.

Consider Fig. 7 where the experimental average stress is plotted against the actual average strain and the predicted average strain. The overall work of adhesion, W_{adh} , is calculated by integrating the experimental load versus displacement curve and dividing by the maximum contact area. This quantity corresponds to the energy required to drive the crack plus the energy dissipated in the bulk of the polymer sample. If we integrate the area under the curve of load versus predicted displacement, we should obtain the energy required to cause adhesive failure if the polymer layer remained linearly elastic. Therefore, the difference between the total energy dissipated and the energy dissipated under the predicted displacement curve corresponds to the energy dissipated in the bulk of the adhesive. To illustrate this point graphically, Fig. 7 shows the area corresponding to the interfacial fracture energy shaded with horizontal lines and the area for bulk deformation energy shaded by vertical. Quantitatively, these energies normalized by the maximum contact area are 11.65 J/m^2 for the interfacial fracture and 15.95 J/m^2 for the bulk energy dissipation. Since the value for the interfacial fraction only accounts for energy associated with the region of the crack tip, the average value for G , 7.94 J/m^2 , also roughly agrees with this average quantity of 11.65

J/m^2 . Additionally, the D/T adhesive in the flat probe test did not surpass the yield point on average; therefore, the value for W_{adh} , 9.75 J/m^2 , also corresponds to the average interfacial fracture energy of 11.65 J/m^2 . Therefore, regardless of the preferred mode of deformation and failure, the energy required to cause adhesive failure, or the local G , is independent of geometry and purely dependent upon the underlying physics of the materials.

B. Adhesive failure analysis of viscoelastic system

Until this point in the article, we have used elasticity arguments to justify the effects of confinement on the mode of failure and have used mostly elastic materials to illustrate our conclusions. Although the D/T samples exhibit high values of adhesion relative to most purely elastic solids, we must address the issue of increased viscoelasticity, since viscous dissipation is known to play an important role in many applications. In the D/T samples, viscoelastic effects are localized near the crack tip region where the local stresses and strain rates are amplified. In this case, the volume of material affected by the viscoelastic properties is small relative to the overall sample dimensions. Apart from the yielding behavior observed at large tensile loads, the response of the bulk of the compliant layer is well represented by linear elasticity. A more complicated analysis is obviously required in situations where the bulk of the material is able to flow at relatively low stresses.^{35,43–45} As we will demonstrate in this section, many of the general features highlighted for more purely elastic materials are still relevant.

As can be seen in Fig. 6, the PEHA sample has a much more predominant viscoelastic character than does the D/T sample. The first evidence for how this characteristic affects the overall adhesion is provided by Figs. 9 and 10, which show the average-stress versus average-strain data for the spherical and flat probe geometries, respectively. As a point of reference, a_{max}/h for the spherical indenter is 5.0 and a_{max}/h for the flat probe is 70. For both tests, the corresponding images show behavior that is indicative of a bulk instability. The instability is bulk fingering in the spherical probe test, and cavitation in the flat probe geometry. These instabilities can be understood in terms of the elastic character of the PEHA.

From the rheological data in Fig. 6, we see that at the low frequencies corresponding to the experimental strain rate of 0.07 s^{-1} , the storage modulus (E') is slightly greater than the loss modulus (E''). This modulus describes the elastic energy stored throughout the bulk of the material, which can somehow be minimized by the release of lateral constraints. As seen in Fig. 3, the experimental conditions place the preferred mode of failure in the bulk instability region, which includes fingering (as observed in the images of Fig. 9). Therefore, in a viscoelastic material, the modes of failure are still determined by elastic restoring forces based on the quasielastic storage of energy in the adhesive layer. Once the mode of failure is induced, its propagation in a viscoelastic solid differs from its propagation in an elastic solid.

Whether the mode of failure is edge crack propagation, fingering, or cavitation, the defect's growth in a viscoelastic

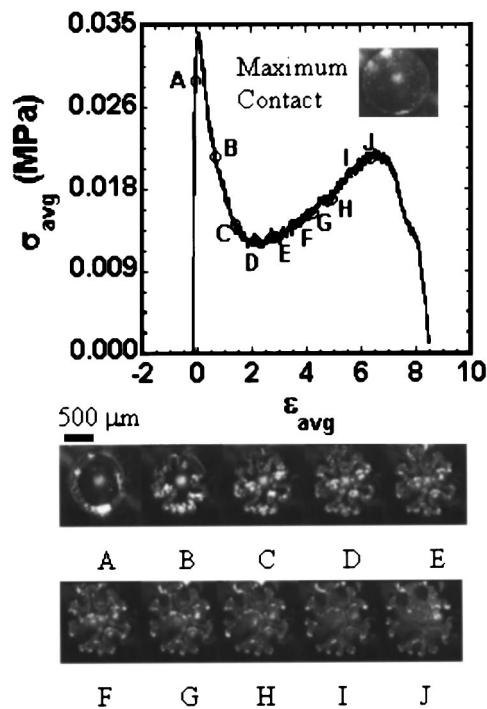


FIG. 9. Average stress-strain curve for a spherical indenter test on PEHA. The maximum a/h is 5.0. Images correspond to the points indicated on the stress-strain curve. Fingers seen in the images occur below the interface as indicated schematically in Fig. 2(d).

solid will be balanced by viscoelastic losses in its vicinity. Defect propagation rates are determined by the rates at which energy is stored elastically and dissipated viscoelastically throughout the sample. In this regime a quantitative evaluation of G becomes impossible analytically because the stress in each point in the viscoelastic material is dependent on the complete load history.³⁵ Nevertheless, for the purpose of comparing the same adhesive on different surfaces or different adhesives on the same surface, some scaling arguments can be developed which correctly predict how the maximum size of the internal cavities should vary with G_0 and with the elastic component E' of the modulus of the adhesive.¹⁴

In the PEHA samples for both geometries, we observe that both the fingering and the cavitation reach a stable sample configuration after initial growth. This stable configuration is essentially a fibrillated state in both tests, where the degree of confinement (effective value of a/h) is close to one. For the spherical probe, one central fibril is pulled and in the flat probe test we observe several fibrils. The progression to a stable configuration is best illustrated by monitoring the distance between cavities in the flat probe geometry. As Fig. 11 shows, the distance between cavities quickly plateaus to a value close to the initial thickness of the film. At that stage there is no longer a driving force to reduce the confinement and we are effectively performing a set of parallel uniaxial tensile tests on the fibrils. The fibrils continue to extend until the applied energy release rate at the polymer/substrate interface surpasses the interfacial fracture criteria or the fibrils extend and finally fail in a cohesive manner.

This stabilization of the fibrils and their subsequent failure illustrate the balance between bulk and interfacial contri-

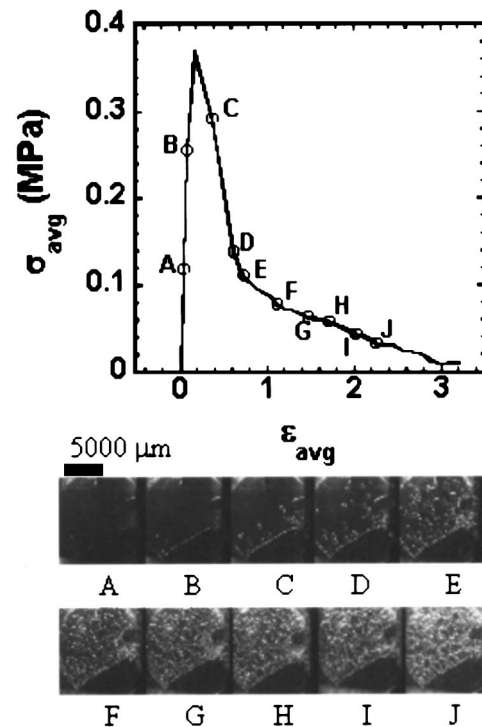


FIG. 10. Average stress-strain curve for a flat indenter test on PEHA. The maximum a/h is 70. Images correspond to the points indicated on the stress-strain curve.

butions to the adhesion of viscoelastic materials. For the PEHA, the interfacial attraction to the steel probe relative to the polymer's stiffness is great enough to allow lateral constraints to develop and force the mode of failure toward a bulk elastic instability. This initial release of lateral constraint does not dissipate much energy by itself, but it allows the sample to reach a configuration where it can be extended past a yield point where higher order dissipation can occur. This higher order dissipation continues until the applied energy release rate in each of the fibrils surpasses the inherent interfacial attraction of the PEHA and steel. This sequence of

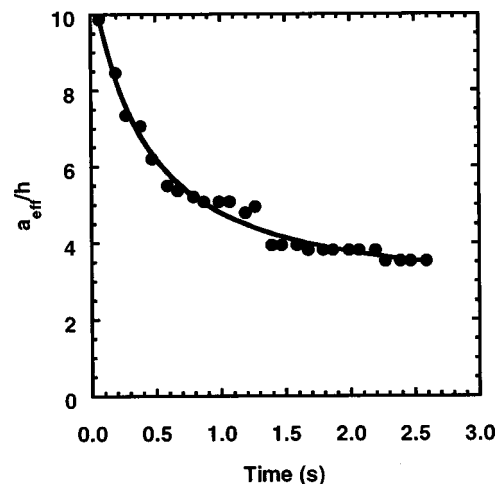


FIG. 11. Average distance between cavities (a_{eff}) normalized by the thickness for the flat indenter test on PEHA. Time is relative to the first occurrence of a cavity.

events is highly conducive to dissipating large quantities of energy and is representative of the behavior of many strong pressure sensitive adhesives.

V. SUMMARY

As a soft, compliant layer is strained in tension, the modes of failure are determined not only by the material properties but also by the degree of confinement imposed by the sample geometry. By understanding how elastic restoring forces develop in confined geometries, we have developed a deformation map defining the regions where bulk shape instabilities or crack propagation will predominate. This analysis has been applied to two different polymer materials that differ greatly in their viscoelastic character. One of the polymers is quite ideally elastic at low strains, whereas the other material has a highly viscoelastic response characteristic of a lightly cross-linked polymer near its gel point.

For both elastic and viscoelastic polymer adhesives, the material physics governing adhesion involve an intricate coupling of bulk and interfacial properties. In the elastic D/T polymer system, we witnessed how different degrees of confinement controlled the rate of release of lateral constraint. In the less confined spherical geometry, the D/T adhesive was allowed to extend past a yield point and increase the effective work of adhesion by a factor of 3. Using linear elastic fracture mechanics, we were able to separate the energy that was used to fracture the interface from the energy that was lost due to yielding the sample. In the flat probe geometry, debonding proceeded from internal defects, and the mode of failure was internal crack propagation. The average amount of energy per unit area required to debond the D/T from the flat probe was roughly equivalent to the interfacial fracture energy in the spherical geometry.

In the PEHA samples, the viscoelasticity balanced the release of lateral constraint and allowed a stable fibrillated structure to develop. This fibrillation process extends the overall work of adhesion and provides a fundamental example of how pressure sensitive adhesives can be optimized to exhibit large adhesive strengths. This example also serves as a framework for future work in continuing to understand how the molecular structure of a polymer adhesive can be used to delicately control the coupling between bulk and interfacial properties.

ACKNOWLEDGMENTS

This work was funded by the NSF under Grant No. DMR-9457923, and by the Western Europe Program of the NSF Division of International Programs. Acknowledgment is also made to the donors of the Petroleum Research Fund for partial support of this work.

¹J. Q. Yao, Proc. Inst. Mech. Eng., Part H **208**, 195 (1994).

²E. Madenci, S. Shkarayev, and R. Mahajan, J. Electron. Packag. Trans. **120**, 336 (1998).

³F. Duval, Ph.D. thesis, Université d'Orléans, 1999.

⁴A. N. Gent and R. P. Petrich, Proc. R. Soc. London, Ser. A **310**, 433 (1969).

⁵Y. Urahama, J. Adhes. **31**, 47 (1989).

⁶A. Zosel, J. Adhes. **34**, 201 (1991).

⁷H. K. Chuang, C. Chiu, and R. Paniagua, Pressure Sensitive Tape Council Annual Technical Seminar, proceedings, 1997, p. 39.

⁸K. R. Shull and A. J. Crosby, J. Eng. Mater. Technol. **119**, 211 (1997).

⁹H. Lakrout, P. Sergot, and C. Creton, J. Adhes. **69**, 307 (1999).

¹⁰J. F. Ganghoffer and A. N. Gent, J. Adhes. **48**, 75 (1995).

¹¹K. J. Wahl, S. V. Stepnowski, and W. N. Unertl, Tribol. Lett. **5**, 103 (1998).

¹²S. A. Syed Asif, K. J. Wahl, and R. J. Colton, Rev. Sci. Instrum. **70**, 2408 (1999).

¹³A. J. Crosby and K. R. Shull, J. Polym. Sci., Part B: Polym. Phys. **37**, 3455 (1999).

¹⁴C. Creton and H. Lakrout, J. Polym. Sci. Part B Polym. Phys. **38**, 965 (2000).

¹⁵A. N. Gent and C. Wang, J. Mater. Sci. **26**, 3392 (1991).

¹⁶K. R. Shull, D. Ahn, W.-L. Chen, C. M. Flanagan, and A. J. Crosby, Macromol. Chem. Phys. **199**, 489 (1998).

¹⁷K. R. Shull, C. M. Flanagan, and A. J. Crosby, Phys. Rev. Lett. **84**, 3057 (2000).

¹⁸D. Ahn and K. R. Shull, Langmuir **14**, 3646 (1998).

¹⁹D. Maugis and M. Barquins, J. Phys. D **11**, 1989 (1978).

²⁰A. N. Gent and S. M. Lai, J. Polym. Sci., Part B: Polym. Phys. **32**, 1543 (1994).

²¹E. H. Andrews and A. J. Kinloch, J. Polym. Sci., Part C: Polym. Symp. **46**, 1 (1974).

²²A. Zosel, J. Adhes. **30**, 135 (1989).

²³A. Zosel, Colloid Polym. Sci. **263**, 541 (1985).

²⁴C. Creton, in *Materials Science and Technology: A Comprehensive Treatment*, Vol. 18: Processing of Polymers, edited by H. E. H. Meijer (VCH, Weinheim, 1997), pp. 707–741.

²⁵S. H. Spiegelberg and G. H. McKinley, J. Non-Newtonian Fluid Mech. **67**, 49 (1996).

²⁶P. G. Saffman and G. I. Taylor, Proc. R. Soc. London, Ser. A **245**, 312 (1958).

²⁷E. Lemaire, P. Levitz, G. Daccord, and H. Vandamme, Phys. Rev. Lett. **67**, 2009 (1991).

²⁸K. R. Shull, D. Ahn and C. Mowery, Langmuir **13**, 1799 (1997).

²⁹A. N. Gent, Rubber Chem. Technol. **67**, 549 (1994).

³⁰A. N. Gent and E. A. Meinecke, Polym. Eng. Sci. **10**, 48 (1970).

³¹G. H. Lindsey, J. Appl. Phys. **38**, 4843 (1967).

³²I. N. Sneddon, Proc. R. Soc. London, Ser. A **187**, 229 (1946).

³³T. Mura, *Micromechanics of Defects in Solids* (Kluwer, Dordrecht, 1993).

³⁴G. Josse and C. Creton, Proceedings of the 23rd Annual Meeting of the Adhesion Society, 2000, p. 36.

³⁵Y. Y. Lin, C. Y. Hui, and J. M. Baney, J. Phys. D **32**, 2250 (1999).

³⁶K. L. Johnson, *Contact Mechanics* (Cambridge University Press, New York, 1985).

³⁷C. Creton and L. Leibler, J. Polym. Sci., Part B: Polym. Phys. **34**, 545 (1996).

³⁸C. Gay and L. Leibler, Phys. Rev. Lett. **82**, 936 (1999).

³⁹K. R. Shull, A. J. Crosby, H. Lakrout, and C. Creton, Proceedings of the 23rd Annual Meeting of the Adhesion Society, 1999, p. 313.

⁴⁰C. L. Mowery, A. J. Crosby, D. Ahn, and K. R. Shull, Langmuir **13**, 6101 (1997).

⁴¹D. Ahn and K. R. Shull, Macromolecules **29**, 4381 (1996).

⁴²C. M. Flanagan, A. J. Crosby, and K. R. Shull, Macromolecules **32**, 7251 (1999).

⁴³A. Falsafi, P. Deprez, F. S. Bates, and M. Tirrell, J. Rheol. **41**, 1349 (1997).

⁴⁴C.-Y. Hui and J. M. Baney, Langmuir **14**, 6570 (1998).

⁴⁵J. M. Baney and C. Y. Hui, J. Appl. Phys. **86**, 4232 (1999).